

Article

Preliminary Studies on Atmospheric Monitoring by Employing a Portable Unmanned Mie-Scattering Scheimpflug Lidar System

Zhi Liu ¹, Limei Li ¹, Hui Li ² and Liang Mei ^{1,*} 

¹ School of Optoelectronic Engineering and Instrumentation Science, Dalian University of Technology, Dalian 116024, China; liuzhi@mail.dlut.edu.cn (Z.L.); llm0424@mail.dlut.edu.cn (L.L.)

² School of Information and Communication Engineering, Dalian University of Technology, Dalian 116024, China; hui.li@dlut.edu.cn

* Correspondence: meiliang@dlut.edu.cn

Received: 16 March 2019; Accepted: 5 April 2019; Published: 8 April 2019



Abstract: A portable unmanned Mie-scattering Scheimpflug lidar system has been designed and implemented for atmospheric remote sensing. The Scheimpflug lidar system employs a continuous-wave high-power 808 nm laser diode as the light source and the emitted laser beam is collimated by an F6 lens with a 100 mm aperture. Atmospheric backscattering light is collected by a F5 lens with a 150 mm aperture and then detected by a 45° tilted image sensor. The separation between the transmitting and the receiving optics is about 756 mm to satisfy the Scheimpflug principle. Unmanned outdoor atmospheric measurements were performed in an urban area to investigate system performance. Localized emissions can be identified by performing horizontal scanning measurements over the urban atmosphere for 107° approximately every 17 min. The temporal variation of the vertical aerosol structure in the boundary layer has also been studied through zenith scanning measurements. The promising result shows great potential of the present portable lidar system for unmanned atmospheric pollution monitoring in urban areas.

Keywords: Scheimpflug lidar; aerosol; pollution; laser diode; boundary layer; atmosphere; remote sensing

1. Introduction

During recent decades, the increasing demand for atmospheric aerosol data has promoted the rapid development of atmospheric lidar techniques. Atmospheric parameters such as aerosol extinction, optical depth, cloud height, boundary layer, microphysical aerosol parameters, etc., can be qualitatively or quantitatively studied by various lidar techniques such as Raman lidar [1–4], high spectral resolution lidar [5,6] and Mie-scattering lidar [7–12]. Among these lidar techniques, the elastic Mie-scattering lidar system, operating at 532/1064 nm based on flash-lamp or diode-laser pumped pulsed Nd:YAG lasers, is the most widely deployed [13,14]. Since 2000, global and regional lidar networks have also been set up to retrieve routine aerosol spatio-temporal distribution, e.g., the European Aerosol Research Lidar Network (EARLINET) [15], the Micro-pulse Lidar Network (MPLNET) [16], and the Asian Dust and Aerosol Lidar Observation Network (AD-NET) [17]. The majority of lidars currently deployed in EARLINET and PollyNET are of the Raman-polarization type [18,19]. National ceilometer networks exist worldwide but are mainly dedicated to cloud layer or mixing layer studies [20–22]. The increasing demands for continuous atmospheric monitoring also place high technical requirements on atmospheric lidar techniques. In particular, lidar systems with untended operation, portability, low-maintenance or even maintenance-free, low cost, eye safe, etc.,

are of great interest for autonomous routine operations as well as lidar networks, and extensive effort has been devoted to this area [23–29].

The Scheimpflug lidar technique has recently been developed for atmospheric aerosol monitoring, combustion diagnostics, etc. [30–40]. The range-resolved atmospheric backscattering signal can be retrieved by a Scheimpflug-principle based imaging system. The cost of the lidar system can be greatly reduced by employing low-cost compact high-power laser diodes as light sources and highly integrated inexpensive image sensors as detectors [31], which are also nearly maintenance free. However, the Scheimpflug lidar systems developed so far are mainly based on off-the-shelf astronomical telescopes and optomechanics, which are inconvenient for field deployment and may require frequent adjustments particularly during outdoor measurements. Thus, a compact, stable, portable and unmanned Scheimpflug lidar system is in great demand for routine atmospheric aerosol measurements and outdoor measurement campaigns. In this work, we report on the development of a portable unmanned Mie-scattering Scheimpflug lidar system based on custom-designed optical architecture and optomechanics, and investigate its feasibility for pollution source tracking as well as vertical aerosol layer structure studies. In the following sections, we will first introduce the portable Scheimpflug lidar system in detail and then investigate the system performance by measuring atmospheric pollution under different atmospheric conditions. Moreover, atmospheric horizontal and zenith scanning measurements have also been performed for preliminary studies on urban pollution source tracking and vertical aerosol structure.

2. Instrumentation

2.1. Optomechanics and Electronics

The system layout as well as the photograph of the Scheimpflug lidar system are shown in Figures 1 and 2, respectively. An 808 nm laser diode with approximately 4 W output power is employed as the light source. The C-mount laser diode is housed by a customized aluminum mount with two thermoelectric coolers (TECs, 20 × 20 mm). A proportional–integral–derivative (PID) based TEC driver is used to control the driving current of the TECs. The case temperature of the laser diode can be stabilized with a precision better than $\pm 0.1^\circ$. Generally speaking, laser diodes have very good power stability and the small temporal fluctuation of the laser output power does not have any significant effect on the signal-to-noise ratio (SNR) of measured lidar signals. The deterioration of performance should be evaluated during long-term operation. The laser diode mount is installed on a customized x-y-z linear translation stage, allowing precision focusing and positioning when collimating the laser beam. The laser beam emitted from the laser diode is folded by an elliptical mirror (52 mm for short axis) and then collimated by a F6 achromatic lens ($\varnothing 100$ mm). A removable 10% reflecting mirror together with a black and white camera are also mounted in the beam path to observe the field-of-view (FOV) of the transmitting optical system during system alignment. All optomechanical components are mounted on an L-shaped aluminum bar, which can be rotated around a rotation stage (Zolix RSM73-1) that is fixed on the baseplate. The angle of the transmitted laser beam to the receiving optics, also referred to as the observation angle, can then be manually adjusted by tuning the rotation stage. The L-shaped aluminum bar can be locked on the baseplate as the Scheimpflug lidar system is well aligned.

Atmospheric backscattering light is received by a F5 achromatic lens ($\varnothing 150$ mm, $f = 750$ mm). The backscattering laser beam is then folded by an elliptical mirror (70 mm short axis). A 45° tilted Complementary Metal-Oxide-Semiconductor (CMOS) sensor (Lumenera, Lt225NIR, 2048 × 1024 pixels) is employed to capture the atmospheric backscattering image. An 808 nm interference filter (Edmund Optics) with 3 nm full width at half maximum (FWHM) and a high-pass color filter (Edmund Optics, RG715) are employed before the CMOS sensor to suppress the sunlight background. Nevertheless, the SNR is dependent on the sunlight shot noise and the photo-response non-uniformity (PRNU) noise after a number of signal averaging processes during daytime, while it is dominated

by the PRNU noise during nighttime. It should be emphasized that the ultimate limit of the SNR is determined by the PRNU noise as the sunlight shot noise is greatly suppressed by performing long-time signal averaging. The tilted CMOS sensor as well as the filters are mounted on a linear translation stage for focusing. A removable beam splitter is placed in the beam path to reflect about 10% of the backscattering light into a black and white camera, which is used for assisting system alignment. By employing a long-pass filter (Edmund Optics, RG780), the measurement scenery as well as the laser beam reflected by a distant hard target, e.g., a tall building, can be observed through the black and white camera even during daytime. The receiving lens is fixed on the front frame, while the elliptical mirror is mounted on the baseplate. A 3D-printed plastic tube and box are fixed on the baseplate to protect the optical path from ambient scattering light. The separation between the optical axis of the transmitting lens and the optical axis of the receiving lens is about 756 mm to satisfy the Scheimpflug principle.

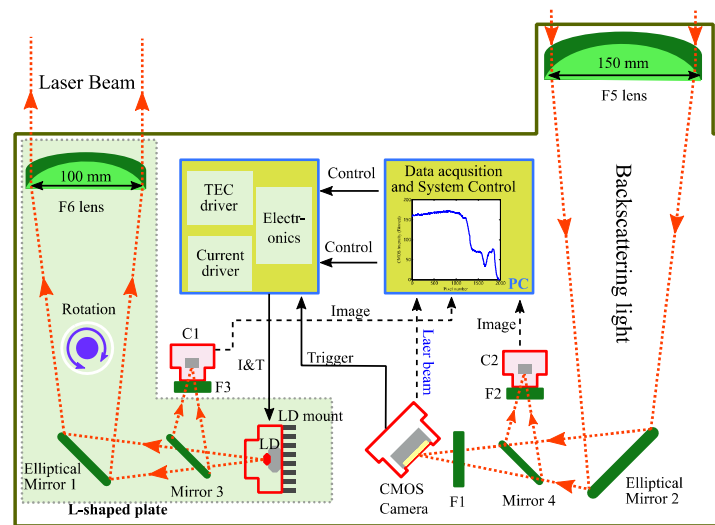


Figure 1. Schematic of the lidar system, LD: laser diode, F1 consists of an 808 nm interference filter and a RG715 long pass filter, F2: RG780 long pass filter, F3: RG780 long pass filter, Mirror 3 and Mirror 4: 10% reflection and 90% transmission mirrors, C1 and C2 are black-white cameras.

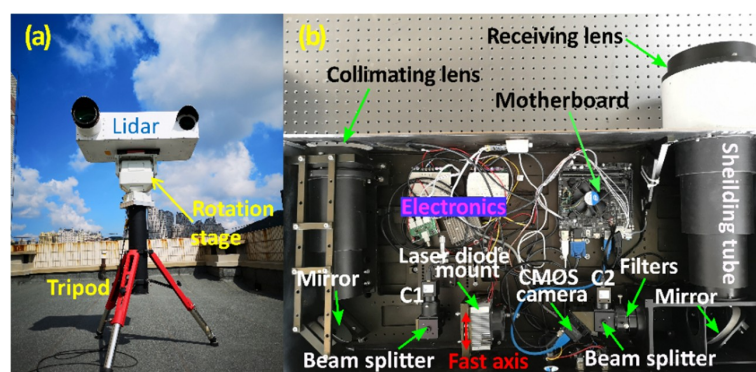


Figure 2. The portable unmanned Scheimpflug lidar system (a) system picture, the system was placed on the 7th floor balcony of an education building in Dalian University of Technology, (b) system layout, the double-end arrow indicates the fast axis of the laser diode.

The current and TEC driving circuits are mounted on the baseplate. A computer is also integrated for system controlling as well as data acquisition. The power supply of the whole lidar system is rated for 24 V, which is down-converted to 12 V to power the motherboard of the computer. The Scheimpflug lidar system has a dimension of $940 \times 450 \times 230$ mm (length \times width \times height) and weight about

30 kg. The lidar system is mounted on a 2-dimensional (2D) large-load rotation stage. The whole lidar system is carried by a tripod shown in Figure 2a. A LabVIEW-based software program has been developed for unmanned automatic atmospheric measurements.

2.2. Signal Acquisition and Processing

As the sunlight background and the dark current signal of the CMOS sensor contribute significantly to the measured lidar signal, the laser diode is turned on and off alternatively by a square-wave modulation signal, which is synchronized with the exposure of the CMOS sensor. Correspondingly, the laser beam image and the background image can be alternately recorded by the CMOS sensor in the region of interest (2048×200 pixels), referred to as the "on-image" and the "off-image", respectively. The full image of the laser beam can be detected without truncation owing to the large detection area of the 2D CMOS sensor. Correspondingly, the geometrical compression factor is equal to one for the full measurement range. The raw lidar signal and the background signal can be obtained by binning the pixel intensities of 200 lines from the on- and off-images, respectively. Background subtraction is performed through signal interpolation to eliminate the contributions from the sunlight background and the dark current [30]. The final lidar signal is then obtained by taking the statistic median value of a number of signals to suppress the temporal noise such as the sunlight shot noise, readout noise and the dark current shot noise, etc. The exposure time of the CMOS sensor automatically changes according to the intensity of the background signal in order to optimize the SNR [41]. Meanwhile, the averaging number also changes correspondingly to maintain the same total measurement time for each single lidar curve, e.g., all lidar signals have been averaged 45 s for static measurements. The Savitzky–Golay (SG) filter, with 8-order polynomial as the fitting function and a frame length of 79 is employed to further improve the SNR. The pixel-distance relationship is calibrated by measuring the backscattering signal from a hard target with a known distance. According to the Scheimpflug principle, the range resolution of the Scheimpflug lidar system in the near range is extraordinarily high, while it decreases rapidly with the measurement distance, as shown later in Figure 3. Thus, signal resampling is also performed for the near range lidar signals (<700 m) [41], and the range resolution is reduced to about 3 m in this region. Nevertheless, the lidar signals were still unequally sampled. The lidar signal has been interpolated with equal sampling distance (i.e., 3 m) from 90 m to 10000 m for the retrieval of the extinction coefficient, while the profile of the lidar signal is retained.

2.3. Pixel-Distance Relationship

In Scheimpflug lidar techniques, the angle between the transmitting optics and the receiving optics, referred to as the observation angle, is rather small, typically less than 1° , which is difficult to measure. A common approach for determining the observation angle is to measure the backscattering signal from a distant hard target, e.g., a tall building located at 1–2 km, the distance of which can be readily measured by a range finder. The observation angle as well as the pixel-distance relationship can then be calibrated from the distance of the tall building and the corresponding pixel position on the image sensor according to geometric optics and the Scheimpflug principle. The typical distance-pixel relationship as well as the range resolution are shown in Figure 3. As can be observed, the measurement distance has a non-linear relationship with the pixel. By taking the differential of the distance-pixel curve, it can be found out that the range resolution increases with the square of the measurement distance. The theoretical range resolutions for the present Scheimpflug lidar system at 1 km, 5 km and 10 km are 7 m, 170 m and 718 m, respectively.

When the portable Scheimpflug lidar system are exposed to strong sunlight during outdoor campaigns, the optical components and the optomechanics could be deformed due to thermal expansion and contraction, which leads to a small variation of the observation angle (typically less than 0.01°). As a result, the atmospheric backscattering image of the transmitted laser beam can shift along the image sensor and the pixel-distance relationship may also change. In other words, the pixel

position of the backscattering echo from the reference building/hard target, denoted as the reference pixel position, could drift back and forth as the temperature changes. Outdoor experiments have been continuously carried out for several days to evaluate the dependency of the drift of the reference pixel position on the system temperature. It has been confirmed that the drifting is generally related to the system temperature. However, no simple function can be derived to describe the relationship as each optical component may have different temperatures and also contribute unequally to the drift. Thus, real-time pixel-distance relationship calibration is performed for outdoor measurements by measuring the pixel position of the backscattering echo from the reference hard target at scheduled times, e.g., every hour.

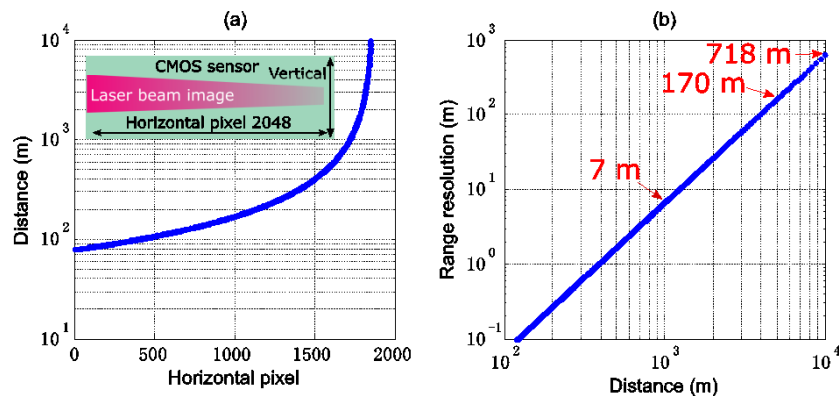


Figure 3. (a) Pixel-distance relationship, the inset figure shows a sketch of the laser beam image recorded by the CMOS sensor, a real laser beam image, measured by a Scheimpflug lidar system with an 800 mm focal length Newtonian telescope, is referred to Figure 7 in [30] (b) range resolution vs. measurement distance. Focal length: 750 mm, tilt angle 45° , pixel pitch $5.5 \mu\text{m}$, number of horizontal pixels 2048, transmitter-receiver separation 756 mm, distance of the calibration target 1308 m, and the pixel position of the backscattering signal from the calibration building is 1750.

3. Measurements

3.1. System Performance Validation

Atmospheric remote measurement was performed on a near horizontal path from 4 to 5 July 2018 in Dalian, Northern China. During this period, the atmosphere is generally clean with only few local emissions. The lidar system was placed on the second-floor balcony of the School of Physics, Dalian University of Technology (DLUT). Although the elevation angle of the lidar system was low, i.e., about 5° , the altitude of the scanning lidar system was far beyond the human height around the measurement site. The PM10 particle concentration increased from $15 \mu\text{g}/\text{m}^3$ to about $50 \mu\text{g}/\text{m}^3$, reported by the Qixianling national pollution monitoring station that is located at about 2.5 km away from the lidar system in the west-southwest direction. Figure 4a shows the temporal-spatial map of the recorded atmospheric backscattering signal. The lidar signals were only about a third of those measured by previous SLidar systems (referred to as Newtonian-SLidar) under similar atmospheric conditions, which employed a commercial Newtonian telescope (200 mm aperture) as the receiver [31]. The lower amplitude of the lidar signal is primarily due to the smaller receiving area of the 150-mm refractor, as well as the low transmittance of refractors with coatings not optimized for near infrared wavelengths. Nevertheless, the SNRs of the lidar signals at around 100 m after about 45 seconds data averaging and signal filtering were beyond 300:1 during nighttime measurements, while it varied between 100 and 300 during daytime measurement depending on the sunlight intensity. The aerosol extinction coefficient can be retrieved according to the Klett method [42] with the boundary value of the extinction coefficient obtained in the far distance where the atmosphere is assumed to be homogeneous by employing the slope method [43]. The maximum retrieval range was set to 7 km. The temporal-spatial distribution of the aerosol extinction coefficient is shown in Figure 4b. Localized pollution, possibly due to vehicle

emissions, appeared from 18:00 on 4 July to around 08:00 on 5 July at around 300 m away from the lidar system.

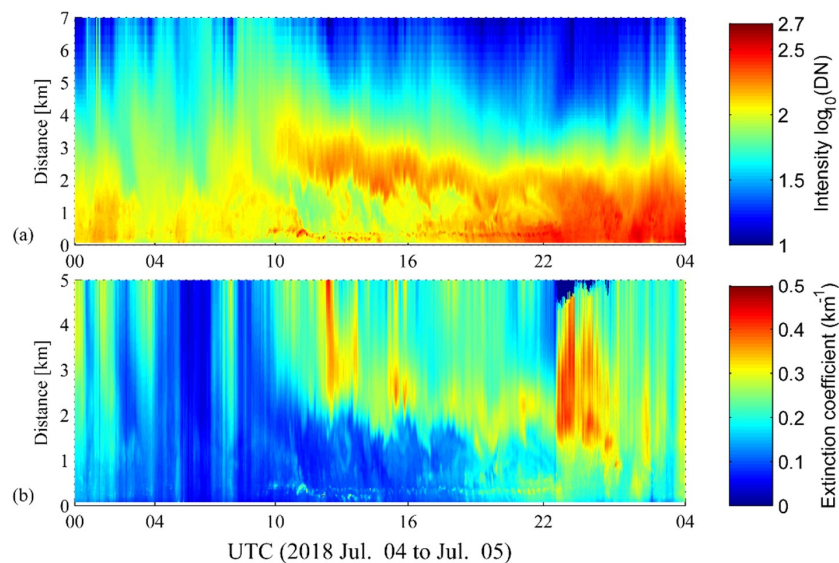


Figure 4. Temporal-spatial map of the (a) received signal intensity and (b) the atmospheric extinction coefficient. The measurements were performed on a near horizontal path with an elevation angle of 5° . Location of the lidar system: $38^\circ 52' 46.4'' \text{N}$ $121^\circ 31' 42.1'' \text{E}$. The local times is 8 h ahead of the Universal Coordinated Time (UTC). DN means digital number of the pixel intensity.

3.2. Atmospheric Horizontal Scanning Measurements for Pollution Source Tracking

Localized emission sources, which are difficult to measure by point monitoring stations due to spatial and temporal averaging, can be identified by scanning lidar measurements. Scanning lidar measurements have been reported in previous work for urban pollution monitoring by employing conventional pulsed lidar systems [24,26,28]. In this work, the portable unmanned Scheimpflug lidar system has also been employed for pollution source tracking in urban areas in Dalian, Northern China. The lidar system was placed on the 7th floor balcony of the education building in DLUT ($38^\circ 53' 00.7'' \text{N}$, $121^\circ 31' 37.2'' \text{E}$). The scanning area of the lidar system ranged from the south to the east direction, covering a range of 107° . As the laser beam could be blocked by surrounded tall buildings, the scanning area was divided into three different sub-regions and the elevation angle of each scanning regions varied between 4.2° to 8.5° to avoid shooting buildings, as shown in Figure 5. The elevation angles for the three measurement regions were 5.5° (region A), 8.5° (region B) and 4.2° (region C), respectively. Two national pollution monitoring stations were located around the scanning area. The Qixianling station was about 3 km away from the lidar system in the south direction and the Xinghai station was about 4 km away from the lidar system in the east direction. Moreover, a Micro-air sensor (Fairsense) was also mounted at 300 m away from the lidar system in the south direction, which is able to measure the PM₁₀/PM_{2.5} concentration every 15 min. During the measurement period, the PM₁₀ concentration generally varied between 30–81 $\mu\text{g}/\text{m}^3$, according to the three measurement stations.

The measurement procedures are summarized as following:

(1) In the beginning of each scanning period, the lidar system will first cruise to the preset calibration position and then measure the backscattering signal from a reference building, the distance of which has been measured by a range finder (1308 m for the present measurements). The distance of the reference building and the corresponding pixel position of the backscattering echo can then be used for the calibration of the pixel-distance relationship for the current scanning period [30].

(2) The lidar system then automatically cruises to the starting position of the scanning area and adjusts the exposure time according to the total incident light intensity. An optimized exposure time can ensure the camera operating under high-light-level condition without saturation. In other words,

the total incident light intensity should be at least more than 10% of the full-well intensity in order to minimize the noise resulting from the PRNU of the image sensor [41]. Typical exposure time is 20 ms under full sunny weather condition and 500 ms for complete darkness. However, the camera may still be saturated due to nearly direct solar radiation just after sunrise.

(3) After the auto-adjustment of the exposure time, the scanning measurement begins. In each scanning region, the elevation angle is constant while the azimuth angle was increased in 1° step. During the transitions of different measurement regions, e.g., from region A to region B, the laser diode is turned off first for security and the lidar system cruises to the starting position of region B. The laser diode is then re-started. The measurement time for each scanning angle is 8 s, and the total measurement for the whole scanning area (249° – 355°) was of about 17 min. The total scanning time is of about one hour for 360° panoramic scan. The lidar curves have been automatically stored in the computer for post-analysis by Matlab-based programs.

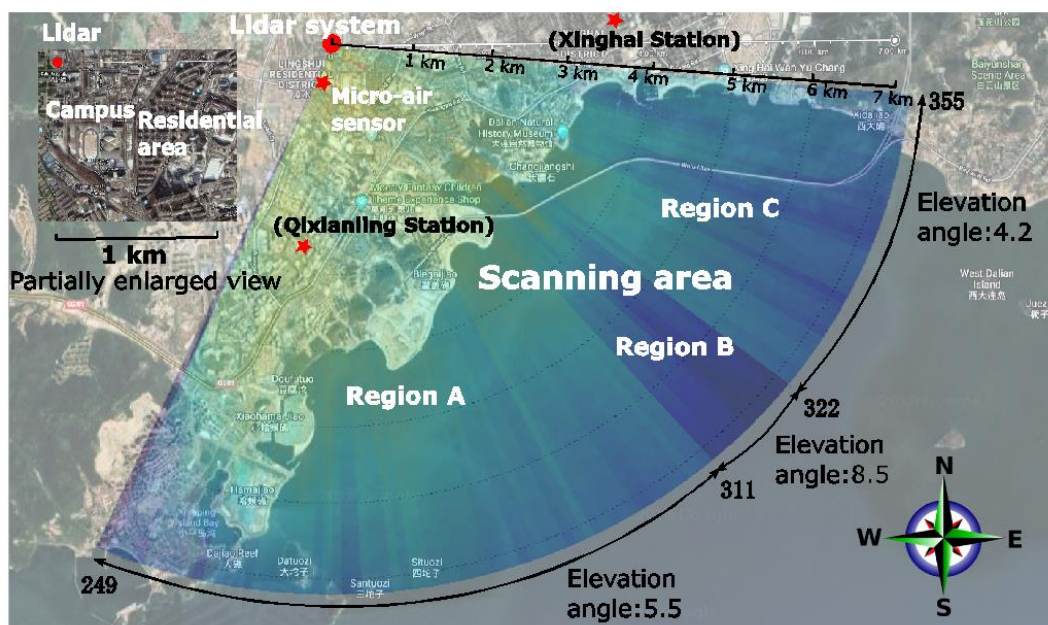


Figure 5. Experimental site map, the SLidar system was placed on the 7th floor balcony of the education building in Dalian University of Technology (DLUT) during the scanning measurements. The Qixianling and Xinghai national pollution monitoring stations can measure the particle concentrations every hour. The Micro-air sensor (Fairsense) was able to measure PM₁₀ and PM_{2.5} concentrations every 15 min. Location of the lidar system: $38^\circ53'00.7''N$, $121^\circ31'37.2''E$. Azimuth angles for regions A, B and C are 249° – 310° , 311° – 321° , 322° – 355° , respectively. The direction of east is defined as 0° .

3.3. Atmospheric Vertical Scanning Measurements

Atmospheric vertical scanning measurements have also been performed from 15 to 16 October 2018 to investigate the vertical atmospheric aerosol structure in the boundary layer. The lidar system, located at the 7th floor balcony of the education building in DLUT, was pointed to the east direction. Limited by the vertical scanning range of the rotation stage and the field of view, the vertical scanning angle ranges from 3° to 36° . The laser beam could shoot on tall buildings with smaller elevation angles. The measurement procedures are similar to the horizontal area scanning discussed in the above section. Atmospheric particulate concentration, e.g., PM₁₀ concentration, was reported by the Xinghai national pollution monitoring station, which was near the laser beam path.

4. Discussion

Figure 6 shows the scanning maps of the atmospheric backscattering signals obtained during different hours from 20 to 21 September. As can be seen, there is a clear boundary between different scanning regions. In particular, the scanning region B that has a much larger elevation angle often shows different backscattering profiles compared with the neighboring scanning regions with lower elevation angles, which implied a vertically layered structure of the atmosphere. However, it does not necessarily mean that upper layers (higher altitude) has larger aerosol load. Localized emission features were mainly observed within 3 km range from the lidar system due to the increased measurement altitude as well as the decreased range resolution for far distance. On the other hand, the area beyond 3 km is mostly the Yellow sea, which does not have specific emission sources.

The aerosol extinction coefficients were retrieved from the lidar profiles in order to better identify the pollution sources. As the lidar system operated in the infrared region, the aerosol extinction coefficient is retrieved according to the Klett method by ignoring the contributions from molecules. The retrieval of the aerosol extinction coefficient for scanning measurements is challenging due to short averaging time and thus lower SNR. The measurement error of the boundary value of the extinction coefficient could lead to large uncertainties on the scanning map of the aerosol extinction coefficient. Thus, the lidar signals in each scanning region have been smoothed by performing spatial averaging along the azimuth direction with 5° window size in this work. The boundary values of the aerosol extinction coefficient were first retrieved for each lidar profile according to the slope method. The maximum retrieval range was set to 7 km. Moreover, spatial averaging on the subsequent five boundary values of the aerosol extinction coefficient in each scanning region were also performed to reduce the uncertainties of the boundary values, which mainly resulted from noise. Finally, the scanning map of the aerosol extinction coefficient is obtained by analyzing each scanning lidar curve according to the Klett inversion algorithm [31], as shown in Figure 7.

At around 12:00 o'clock on 20 September, the PM₁₀ concentrations reported by the Xinghai station and the Micro-air sensor were about $40 \mu\text{g}/\text{m}^3$ and $60 \mu\text{g}/\text{m}^3$, respectively. Nevertheless, localized high values of the aerosol extinction coefficient can be found at many places, even in the area of the Yellow sea due to frequent human activities during daytime. The low-altitude pollution particles observed in the sea area were most likely due to the horizontal transportation of terrestrial emissions from Dalian city. The swift change of the aerosol extinction coefficient shown in Figure 7a and b could be due to the sea-land breeze. However, we are lacking meteorological data to further verify the transportation and swift variation. Another interesting phenomenon shown in Figure 7a and c was that large aerosol extinction coefficients were both found in region A and C, but not in the region B that has a larger elevation angle and thus a higher measurement altitude. This indicated that the pollutants were mainly concentrated in the altitude below 300 m. In the afternoon of 20 September, emissions can still be observed at around 15:00 due to road/building construction, etc. Nevertheless, the atmosphere gradually became cleaner and only light pollution sources could be observed, as shown in Figure 7d. At around 19:00 in the evening, near range emissions could be readily identified around the university campus and the residential area, which were mainly due to domestic/catering emissions, rush-hour traffic, etc. The PM₁₀ concentration even reached up to $81 \mu\text{g}/\text{m}^3$ according to the nearby Micro-air sensor that was located about 300 m away from the lidar system in the south direction. After this period, the atmosphere became nearly homogeneous due to aerosol mixing in the urban/coastal atmosphere with a wind speed of about 5 m/s. The median value of the aerosol extinction coefficient shown in Figure 7f was about 0.12 km^{-1} , and the PM₁₀ concentration was about $30 \mu\text{g}/\text{m}^3$ according to the Qixianling station and the Micro-air sensor. Since midnight, the planetary boundary layer started to collapse. A clean layer was gradually formed between 220 m and 440 m in the boundary layer, while a residual layer that was due to the turbulence of the previous day appeared beyond the altitude of about 440 m, as can be seen in Figure 7g. A similar phenomenon can also be observed during the vertical scanning measurements. Video 1 shows the temporal variation of the aerosol extinction

coefficient for the scanning area, from which the evolution of the localized pollutions as well as the vertical aerosol structure can be explicitly observed.

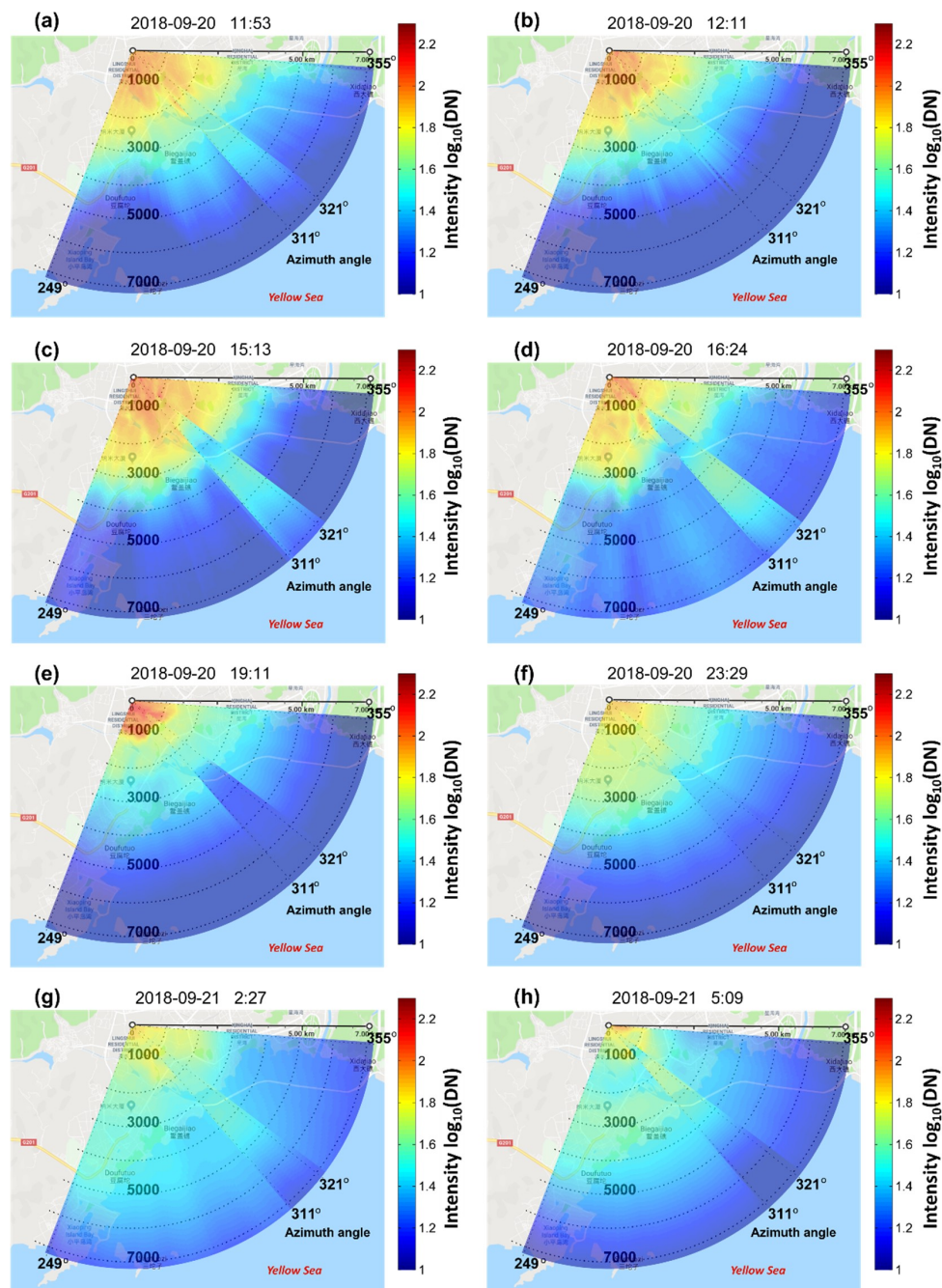


Figure 6. Horizontal scanning map of the received signal intensity measured at (a) 11:53, 2018-09-20, (b) 12:11, 2018-09-20, (c) 15:13, 2018-09-20, (d) 16:24 2018-09-20, (e) 19:11 2018-09-20, (f) 01:22, 2018-09-20, (g) 02:27, 2018-09-21, and (h) 05:09, 2018-09-21. Location of the lidar system: $38^{\circ}53'00.7''\text{N}$, $121^{\circ}31'37.2''\text{E}$. The local times indicated in the sub figures are 8 h ahead of the Universal Coordinated Time (UTC). DN means digital number of the pixel intensity.

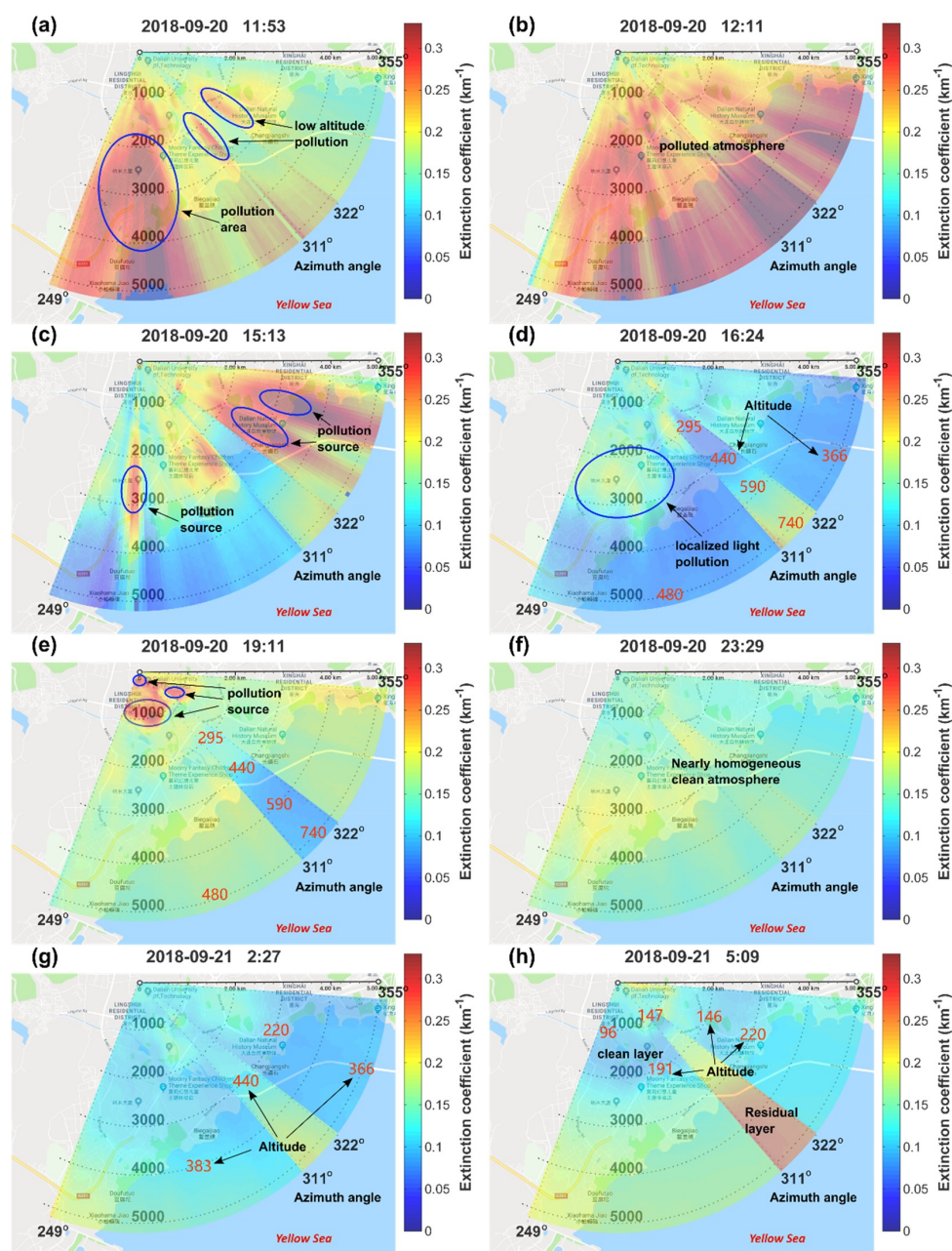


Figure 7. Horizontal scanning map of the atmospheric extinction coefficient measured at (a) 11:53, 2018-09-20, (b) 12:11, 2018-09-20, (c) 15:13, 2018-09-20, (d) 16:24 2018-09-20, (e) 19:11 2018-09-20, (f) 01:22, 2018-09-20, (g) 02:27, 2018-09-21, and (h) 05:09, 2018-09-21. Location of the lidar system: $38^{\circ}53'00.7''\text{N}$, $121^{\circ}31'37.2''\text{E}$. The local times indicated in the sub figures are 8 h ahead of the Universal Coordinated Time (UTC).

Figure 8 shows the vertical scanning signal intensities recorded under different weather conditions. The vertical scanning measurements started at 17:20 on 15 October 2018, when a severe haze was going to occur and the PM_{10} concentration increased up to $224 \mu\text{g}/\text{m}^3$ at 20:00 during the nighttime. As can be seen from Figure 8a and b, the lidar signals with lower elevation angles attenuated much faster, which implied that the pollutants were mainly concentrated at low altitude. After midnight, the northeast wind (level 4 to 6) blows away the pollutants and the PM_{10} concentration decreased to $40\text{--}50 \mu\text{g}/\text{m}^3$. Meanwhile, an optically thin layer was gradually formed between 0.5–1.0 km, as shown in Figure 8d. About one hour later, a clean layer was formed between 0.3–0.8 km altitudes

at 02:40 and a residual layer appeared above the clean layer. During the daytime, solar heating of the surface intensified thermal convection and mixing of air in the boundary layer, which resulted in the expansion of the boundary layer and the clean layer disappeared, as can be seen from Figure 8f. After 14:00 on 16 October, the atmosphere was very clean and the PM10 concentration was of about $20 \mu\text{g}/\text{m}^3$. Meanwhile, the aerosol load was mainly concentrated below 0.6 km, indicating a planetary boundary layer height of approximately 0.6 km, as shown in Figure 8h. Beyond the boundary layer, the atmosphere was very clean and mainly dominated by molecules. Moreover, a thick cloud layer could be observed in the height of about 3 km. Video 2 shows the temporal variations of the backscattering intensities during the vertical scanning measurements.

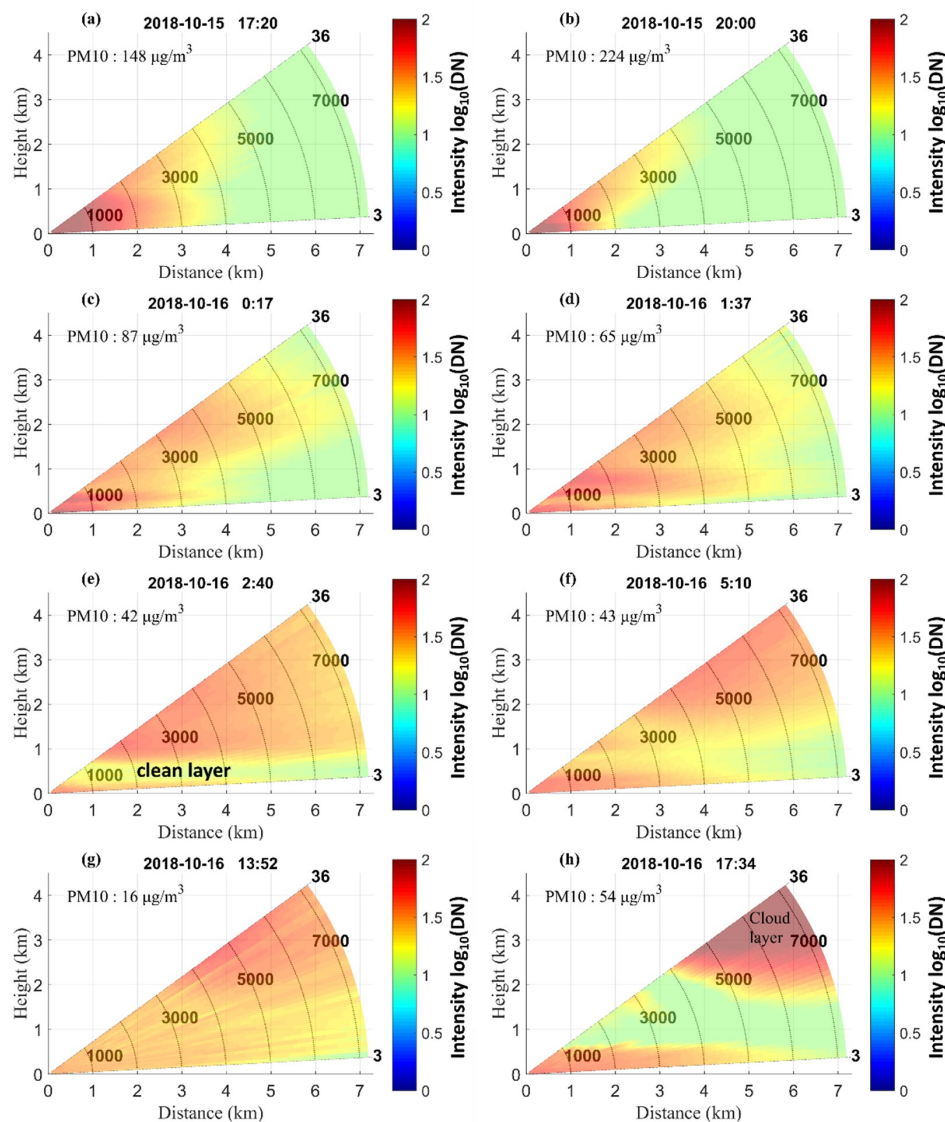


Figure 8. Vertical scanning map of the received signal intensities recorded at (a) 17:20, 15 October, (b) 20:00, 15 October, (c) 00:17, 16 October, (d) 01:37, 16 October, (e) 02:40 16 October, (f) 05:10 16 October, (g) 13:52 16 October, (h) 17:34 16 October. The lidar signals were plotted in log-scale. The PM10 concentrations were measured by the Xinghai national pollution monitoring station. Location of the lidar system: $38^{\circ}53'00.7''\text{N}$, $121^{\circ}31'37.2''\text{E}$. Zenith scanning range: 3° – 36° . The local times indicated in the sub figures are 8 h ahead of the Universal Coordinated Time (UTC). DN means digital number of the pixel intensity.

5. Conclusions

A low-cost unmanned SLidar system, employing high-power continuous wave laser diodes and CMOS image sensors, has been successfully developed for atmospheric remote sensing. The SLidar system is fulfilled by integrating custom designed optomechanics and optoelectronics; 360° panoramic horizontal scanning and 0°–36° vertical scanning are feasible through a large-load rotation stage. Meanwhile, automatic calibration measurement of pixel-distance relationship and automatic setting of the exposure time have been implemented for outdoor autonomous measurements. Unmanned operation is achieved by a custom-designed LabVIEW-based program. The SLidar system is capable of operating during light precipitation conditions. Due to the small receiving aperture of the F5 refractor (150 mm) and its transmission losses, the signal intensity measured by the present SLidar system is of only about a third of that measured by the Newtonian-SLidar system that employs a 200 mm Newtonian telescope as the receiver and a 100 mm refractor (F6) for laser beam collimation under the same weather conditions [31]. Improvements on the signal intensity and thus the SNR should be pursued in future work. Image sensors with higher quantum efficiency (>40%) or larger full-well capacity allowing longer exposure time can further improve the SNR.

Outdoor atmospheric scanning measurements were successfully carried out in September and October 2018. Local emissions due to constructions, catering and traffics etc. can be identified through horizontal scanning measurements. However, as the elevation angle of the horizontal scanning was still a bit high (4.2°–8.5°), ground-level emissions at far distance (>1 km) were rather difficult to detect. The SLidar system should be placed at a higher altitude but with lower elevation angles (e.g., zero degree) can be conceived for future pollution source tracking measurements. Lacking of meteorological data prevents in-depth analysis about the transportation and variations of atmospheric pollutions during the measurement period. Thus, meteorological instruments such as a radiosonde, anemometer around the beach, etc., should be deployed to improve the explanation of the measurement results in future work. In this work, the aerosol extinction coefficient in the horizontal scanning measurements has been retrieved according to the Klett-inversion algorithm with the boundary values of the extinction coefficient obtained from the slope method. Furthermore, spatial averaging has been performed on the original lidar signal as well as the boundary values, which can greatly improve the stability of the inversion. Nevertheless, developing an automatic and robust inversion algorithm, which is suitable for the retrieval of the aerosol extinction coefficient in various situations of scanning measurements has been a big challenge that needs attention in the future. On the other hand, the extinction coefficient could not be retrieved in the vertical scanning measurements in the present work, as the boundary value of the extinction coefficient is difficult to obtain due to the presence of clouds and limited measurement range of the Scheimpflug lidar system, etc.

6. Patents

Liang Mei and Zhi Liu, A new lidar system based on the Scheimpflug principle, 2018-05-16, CN201810497158.2, China.

Supplementary Materials: The following are available online at <http://www.mdpi.com/2072-4292/11/7/837/s1>, <http://www.mdpi.com/2072-4292/11/7/837/s2>, Video S1 and Video S2.

Author Contributions: Conceptualization, L.M.; methodology, Z.L. and L.L.; validation, Z.L. and L.L.; investigation, Z.L. and L.L.; resources, L.L.; data curation, Z.L.; writing—original draft preparation, Z.L. and L.M.; writing—review and editing, H.L. and L.M.; visualization, Z.L. and L.M.; supervision, L.M.; project administration, L.M.; funding acquisition, L.M. and H.L.

Funding: This research was funded by National key research and development program of China, grant number 2016YFC0200600, National Natural Science Foundation of China, grant number 61705030, 61601079, Natural Science Foundation of Liaoning Province, China, grant number 201602163, 20170540169, Fundamental Research Funds for the Central Universities grant number DUT18JC22, and China Postdoctoral Science Foundation, grant number 2018M631779.

Acknowledgments: The authors are grateful to Zheng Kong, Teng Ma, Qingqing Lu, Ruonan Fei, and Guangyu Zhao for their kind help on the system development and outdoor experiments. The authors also acknowledge Weilong Liu, Baosuo Jia, and Yanchao Li for their valuable help in the development of the lidar system and the software program.

Conflicts of Interest: The authors declare no conflict of interest.

References

1. Engelmann, R.; Kanitz, T.; Baars, H.; Heese, B.; Althausen, D.; Skupin, A.; Wandinger, U.; Komppula, M.; Stachlewska, I.S.; Amiridis, V.; et al. The automated multiwavelength Raman polarization and water-vapor lidar Polly(XT): The neXT generation. *Atmos. Meas. Tech.* **2016**, *9*, 1767–1784. [[CrossRef](#)]
2. Radlach, M.; Behrendt, A.; Wulfmeyer, V. Scanning rotational Raman lidar at 355 nm for the measurement of tropospheric temperature fields. *Atmos. Chem. Phys.* **2008**, *8*, 159–169. [[CrossRef](#)]
3. Mamouri, R.E.; Papayannis, A.; Amiridis, V.; Muller, D.; Kokkalis, P.; Rapsomanikis, S.; Karageorgos, E.T.; Tsaknakis, G.; Nenes, A.; Kazadzis, S.; et al. Multi-wavelength Raman lidar, sun photometric and aircraft measurements in combination with inversion models for the estimation of the aerosol optical and physico-chemical properties over Athens, Greece. *Atmos. Meas. Tech.* **2012**, *5*, 1793–1808. [[CrossRef](#)]
4. Wu, S.H.; Song, X.Q.; Liu, B.Y.; Dai, G.Y.; Liu, J.T.; Zhang, K.L.; Qin, S.G.; Hua, D.X.; Gao, F.; Liu, L.P. Mobile multi-wavelength polarization Raman lidar for water vapor, cloud and aerosol measurement. *Opt. Express* **2015**, *23*, 33870–33892. [[CrossRef](#)]
5. Rogers, R.R.; Hair, J.W.; Hostetler, C.A.; Ferrare, R.A.; Obland, M.D.; Cook, A.L.; Harper, D.B.; Burton, S.P.; Shinozuka, Y.; McNaughton, C.S.; et al. NASA LaRC airborne high spectral resolution lidar aerosol measurements during MILAGRO: Observations and validation. *Atmos. Chem. Phys.* **2009**, *9*, 4811–4826. [[CrossRef](#)]
6. Muller, D.; Hostetler, C.A.; Ferrare, R.A.; Burton, S.P.; Chemyakin, E.; Kolgotin, A.; Hair, J.W.; Cook, A.L.; Harper, D.B.; Rogers, R.R.; et al. Airborne Multiwavelength High Spectral Resolution Lidar (HSRL-2) observations during TCAP 2012: Vertical profiles of optical and microphysical properties of a smoke/urban haze plume over the northeastern coast of the US. *Atmos. Meas. Tech.* **2014**, *7*, 3487–3496. [[CrossRef](#)]
7. Sun, W.B.; Hu, Y.X.; MacDonnell, D.G.; Weimer, C.; Baize, R.R. Technique to separate lidar signal and sunlight. *Opt. Express* **2016**, *24*, 12949–12954. [[CrossRef](#)]
8. Marchant, C.C.; Wilkerson, T.D.; Bingham, G.E.; Zavyalov, V.V.; Andersen, J.M.; Wright, C.B.; Cornelsen, S.S.; Martin, R.S.; Silva, P.J.; Hatfield, J.L. Aglite lidar: A portable elastic lidar system for investigating aerosol and wind motions at or around agricultural production facilities. *J. Appl. Remote Sens.* **2009**, *3*, 033511. [[CrossRef](#)]
9. Behrendt, A.; Pal, S.; Wulfmeyer, V.; Valdebenito, A.M.; Lammel, G. A novel approach for the characterization of transport and optical properties of aerosol particles near sources—Part I: Measurement of particle backscatter coefficient maps with a scanning UV lidar. *Atmos. Environ.* **2011**, *45*, 2795–2802. [[CrossRef](#)]
10. Stachlewska, I.S.; Neuber, R.; Lampert, A.; Ritter, C.; Wehrle, G. AMALi—The Airborne Mobile Aerosol Lidar for Arctic research. *Atmos. Chem. Phys.* **2010**, *10*, 2947–2963. [[CrossRef](#)]
11. Dubey, P.K.; Jain, S.L.; Arya, B.C.; Ahammed, Y.N.; Kumar, A.; Shukla, D.K.; Kulkarni, P.S. Indigenous design and development of a micro-pulse lidar for atmospheric studies. *Int. J. Remote Sens.* **2011**, *32*, 337–351. [[CrossRef](#)]
12. Sicard, M.; Izquierdo, R.; Alarcon, M.; Belmonte, J.; Comeron, A.; Baldasano, J.M. Near-surface and columnar measurements with a micro pulse lidar of atmospheric pollen in Barcelona, Spain. *Atmos. Chem. Phys.* **2016**, *16*, 6805–6821. [[CrossRef](#)]
13. Parracino, S.; Richetta, M.; Gelfusa, M.; Malizia, A.; Bellecci, C.; de Leo, L.; Perrimezzi, C.; Fin, A.; Forin, M.; Giappiccucci, F.; et al. Real-time vehicle emissions monitoring using a compact LiDAR system and conventional instruments: First results of an experimental campaign in a suburban area in southern Italy. *Opt. Eng.* **2016**, *55*, 103107. [[CrossRef](#)]
14. Xie, H.L.; Zhou, T.; Fu, Q.; Huang, J.P.; Huang, Z.W.; Bi, J.R.; Shi, J.S.; Zhang, B.D.; Ge, J.M. Automated detection of cloud and aerosol features with SACOL micro-pulse lidar in northwest China. *Opt. Express* **2017**, *25*, 30732–30753. [[CrossRef](#)] [[PubMed](#)]

15. Pappalardo, G.; Amodeo, A.; Apituley, A.; Comeron, A.; Freudenthaler, V.; Linne, H.; Ansmann, A.; Bosenberg, J.; D'Amico, G.; Mattis, I.; et al. EARLINET: Towards an advanced sustainable European aerosol lidar network. *Atmos. Meas. Tech.* **2014**, *7*, 2389–2409. [[CrossRef](#)]
16. Lewis, J.R.; Campbell, J.R.; Welton, E.J.; Stewart, S.A.; Haftings, P.C. Overview of MPLNET, Version 3, Cloud Detection. *J. Atmos. Ocean Tech.* **2016**, *33*, 2113–2134. [[CrossRef](#)]
17. Nishizawa, T.; Sugimoto, N.; Matsui, I.; Shimizu, A.; Higurashi, A.; Jin, Y. The Asian dust and aerosol lidar observation network (Ad-Net): Strategy and progress. *Epj Web Conf.* **2016**, *119*, 19001. [[CrossRef](#)]
18. Baars, H.; Kanitz, T.; Engelmann, R.; Althausen, D.; Heese, B.; Komppula, M.; Preissler, J.; Tesche, M.; Ansmann, A.; Wandinger, U.; et al. An overview of the first decade of Polly(NET): An emerging network of automated Raman-polarization lidars for continuous aerosol profiling. *Atmos. Chem. Phys.* **2016**, *16*, 5111–5137. [[CrossRef](#)]
19. Wandinger, U.; Freudenthaler, V.; Baars, H.; Amodeo, A.; Engelmann, R.; Mattis, I.; Gross, S.; Pappalardo, G.; Giunta, A.; D'Amico, G.; et al. EARLINET instrument intercomparison campaigns: Overview on strategy and results. *Atmos. Meas. Tech.* **2016**, *9*, 1001–1023. [[CrossRef](#)]
20. Caicedo, V.; Rappengluck, B.; Lefer, B.; Morris, G.; Toledo, D.; Delgado, R. Comparison of aerosol lidar retrieval methods for boundary layer height detection using ceilometer aerosol backscatter data. *Atmos. Meas. Tech.* **2017**, *10*, 1609–1622. [[CrossRef](#)]
21. Peng, J.; Grimmond, C.S.B.; Fu, X.S.; Chang, Y.Y.; Zhang, G.L.; Guo, J.B.; Tang, C.Y.; Gao, J.; Xu, X.D.; Tan, J.G. Ceilometer-based analysis of Shanghai's boundary layer height under rain- and fog-free conditions. *J. Atmos. Ocean Tech.* **2017**, *34*, 749–764. [[CrossRef](#)]
22. Adam, M.; Turp, M.; Horseman, A.; Ordonez, C.; Buxmann, J.; Sugier, J. From operational ceilometer network to operational lidar network. *Epj Web Conf.* **2016**, *119*, 27007. [[CrossRef](#)]
23. Spuler, S.M.; Mayor, S.D. Scanning eye-safe elastic backscatter lidar at 1.54 μm . *J. Atmos. Ocean Tech.* **2004**, *22*, 696. [[CrossRef](#)]
24. He, T.Y.; Stanic, S.; Gao, F.; Bergant, K.; Veberic, D.; Song, X.Q.; Dolzan, A. Tracking of urban aerosols using combined LIDAR-based remote sensing and ground-based measurements. *Atmos. Meas. Tech.* **2012**, *5*, 891–900. [[CrossRef](#)]
25. Strawbridge, K.B. Developing a portable, autonomous aerosol backscatter lidar for network or remote operations. *Atmos. Meas. Tech.* **2013**, *6*, 801–816. [[CrossRef](#)]
26. Xie, C.B.; Zhao, M.; Wang, B.X.; Zhong, Z.Q.; Wang, L.; Liu, D.; Wang, Y.J. Study of the scanning lidar on the atmospheric detection. *J. Quant. Spectrosc. Rad. Transf.* **2015**, *150*, 114–120. [[CrossRef](#)]
27. Chiang, C.W.; Das, S.K.; Chiang, H.W.; Nee, J.B.; Sun, S.H.; Chen, S.W.; Lin, P.H.; Chu, J.C.; Su, C.S.; Su, L.S. A new mobile and portable scanning lidar for profiling the lower troposphere. *Geosci. Instrum. Meth.* **2015**, *4*, 35–44. [[CrossRef](#)]
28. Weekley, R.A.; Goodrich, R.K.; Cornman, L.B. Aerosol plume detection algorithm based on image segmentation of scanning atmospheric lidar data. *J. Atmos. Ocean Tech.* **2016**, *33*, 697–712. [[CrossRef](#)]
29. De Wekker, S.F.J.; Mayor, S.D. Observations of Atmospheric Structure and Dynamics in the Owens Valley of California with a Ground-Based, Eye-Safe, Scanning Aerosol Lidar. *J. Appl. Meteorol. Clim.* **2009**, *48*, 1483–1499. [[CrossRef](#)]
30. Mei, L.; Brydegaard, M. Atmospheric aerosol monitoring by an elastic Scheimpflug lidar system. *Opt. Express* **2015**, *23*, 247841. [[CrossRef](#)]
31. Mei, L.; Guan, P.; Yang, Y.; Kong, Z. Atmospheric extinction coefficient retrieval and validation for the single-band Mie-scattering Scheimpflug lidar technique. *Opt. Express* **2017**, *25*, A628–A638. [[CrossRef](#)]
32. Mei, L.; Guan, P. Development of an atmospheric polarization Scheimpflug lidar system based on a time-division multiplexing scheme. *Opt. Lett.* **2017**, *42*, 3562–3565. [[CrossRef](#)]
33. Sun, G.D.; Qin, L.A.; Hou, Z.H.; Jing, X.; He, F.; Tan, F.F.; Zhang, S.L. Small-scale Scheimpflug lidar for aerosol extinction coefficient and vertical atmospheric transmittance detection. *Opt. Express* **2018**, *26*, 7423–7436. [[CrossRef](#)]
34. Brydegaard, M.; Gebru, A.; Svanberg, S. Super resolution laser radar with blinking atmospheric particles—Application to interacting flying insects. *PIER* **2014**, *147*, 141–151. [[CrossRef](#)]
35. Malmqvist, E.; Brydegaard, M.; Alden, M.; Bood, J. Scheimpflug Lidar for combustion diagnostics. *Opt. Express* **2018**, *26*, 14842–14858. [[CrossRef](#)]

36. Brydegaard, M.; Malmqvist, E.; Jansson, S.; Larsson, J.; Torok, S.; Zhao, G.Y. The Scheimpflug lidar method. *Proc. Spie* **2017**, *10406*, 104060I.
37. Brydegaard, M.; Larsson, J.; Török, S.; Malmqvist, E.; Zhao, G.; Jansson, S.; Andersson, M.; Svanberg, S.; Åkesson, S.; Laurell, F.; et al. Short-wave infrared atmospheric Scheimpflug lidar. In Proceedings of the EPJ Web of Conferences, Bucharest, Romania, 25–30 June 2017.
38. Mei, L.; Kong, Z.; Liu, Z.; Zhang, L.; Guan, P. Atmospheric pollution monitoring by employing a 450-nm Scheimpflug lidar system. *Sensors* **2018**, *18*, 1880.
39. Mei, L.; Kong, Z.; Ma, T. Dual-wavelength Mie-scattering Scheimpflug lidar system developed for the studies of the aerosol extinction coefficient and the Angstrom exponent. *Opt. Express* **2018**, *26*, 31942–31956. [[CrossRef](#)]
40. Mei, L.; Guan, P.; Kong, Z. Remote sensing of atmospheric NO₂ by employing the continuous-wave differential absorption lidar technique. *Opt. Express* **2017**, *25*, A953–A962. [[CrossRef](#)]
41. Mei, L.; Zhang, L.; Kong, Z.; Li, H. Noise modeling, evaluation and reduction for the atmospheric lidar technique employing an image sensor. *Opt. Commun.* **2018**, *426*, 463–470. [[CrossRef](#)]
42. Klett, J.D. Lidar inversion with variable backscatter extinction ratios. *Appl. Opt.* **1985**, *24*, 1638–1643. [[CrossRef](#)]
43. Kovalev, V.A.; Eichinger, W.E. *Elastic Lidar: Theory, Practice, and Analysis Methods*; John Wiley & Sons: Hoboken, NJ, USA, 2004.



© 2019 by the authors. Licensee MDPI, Basel, Switzerland. This article is an open access article distributed under the terms and conditions of the Creative Commons Attribution (CC BY) license (<http://creativecommons.org/licenses/by/4.0/>).